Optimizing one-dimensional TiO2 for photocatalytic hydrogen production from a water-ethanol mixture and other electron donors

Tao Peng, Jian Zhang, Srimanta Ray, Fatemeh Saadat Ghareh Bagh, Houssam Fakhouri, Farzaneh Arefi-Khonsari, Jerald A Lalman

Optimizing one-dimensional TiO_2 for photocatalytic hydrogen production from a water-ethanol mixture and other electron donors

Tao Peng[a,b], Jian Zhang[d], Srimanta Ray[c], Fatemeh Saadat Ghareh Bagh[a], Houssam Fakhouri[b], Farzaneh Arefi-Khonsari[b,#], Jerald A. Lalman[a,##]

[a]Department of Civil and Environmental Engineering, University of Windsor, 401 Sunset Ave., Windsor, Ontario N9B 3P4, Canada

[b]Laboratoire Interfaces et Systèmes Electrochimiques (LISE), Centre national de la recherche scientifique (CNRS), Sorbonne Université, Paris F-75005, France

[c]Department of Chemical Engineering, National Institute of Technology Agartala, Tripura, India, 799055

[d]State Key Laboratory of Material Processing and Die and Mould Technology, School of Materials Science and Engineering, Huazhong University of Science and Technology, Wuhan 430074, China

[#]Farzaneh Arefi-Khonsari, Voice: +33-144276815; Fax: +33-144276813; Email: farzaneh.arefi@upmc.fr

[##]Jerald A. Lalman, Voice: +1-519-253-3000 ext. 2519; Fax + 1-519-971-3686; Email: lalman@uwindsor.ca

Abstract

This work is focused on synthesizing and employing one-dimensional (1D) titanium dioxide (TiO_2) for hydrogen (H_2) production. Based on using electron donors (EDs) (ethanol, methanol, fomic acid and 1,2,3 propanetriol), the increased H_2 production, when compared to P25 TiO_2 nanoparticles, was due to the large specific surface area (SSA) and enhanced electron mobility of 1D TiO_2. The impact of the 1D TiO_2 synthesis reaction conditions (temperature, NaOH concentration and the TiO_2 precursor concentration) on the photocatalytic H_2 production rate was evaluated using a 3-factor 3-level Box Behnken design (BBD). The BBD model demonstrated that the temperature and the NaOH concentration significantly affected the 1D TiO_2 phase structure, crystal size, SSA, bandgap and the photocatalytic H_2 production rate. The phase structure and crystal size of 1D TiO_2 were key factors affecting the H_2 production rate. 1D TiO_2 containing an anatase phase with a mean crystal size of 20.1±0.2 nm was synthesized at 126°C, 15 M NaOH and 49 $g \cdot L^{-1}$ TiO_2. The maximum H_2 production rate of 475±12 $\mu mol \cdot h^{-1}$ (quantum efficiency (ε) = 20.2±0.5%) for the 1D TiO_2 sample was significantly enhanced when compared to commercial TiO_2 P25. The H_2 production rate for the optimized 1D TiO_2 was significantly enhanced by decorating the structure with Pt and Au. Hydrothermal synthesized of 1D TiO_2 provided an efficient and low cost method for producing H_2 from ethanol, methanol, fomic acid and 1,2,3 propanetriol.

Key words: 1D titanium dioxide, photocatalyst, anatase, TiO_2-B, hydrothermal, hydrogen production, quantum yield.

1. Introduction

Hydrogen is considered as a promising fuel for the future. 1D TiO_2 nanomaterials have shown significant potential in producing H_2 because of their high electron mobility, large SSA and high mechanical strength [1-5]. Producing 1D TiO_2 using the alkaline hydrothermal method is a relatively facile process with advantages of large-scale production and varied crystal phase [1, 2, 4-11]. In studies employing the hydrothermal method, 1D TiO_2 nanomaterials containing anatase [1, 12] or TiO_2-B [10, 11] were produced under selected synthesis conditions. These materials have been utilized to produce hydrogen (H_2) from the photocatalytic splitting of water or from other substrates such as ethanol [10, 13]. In comparison to TiO_2 nanoparticles, studies have reported improved H_2 production from ethanol under UV light conditions when employing 1D TiO_2 [10, 13]. Hydrothermal synthesis factors such as reaction temperature and the TiO_2-to-NaOH molar ratio can significantly affect the 1D TiO_2 phase structure, crystal size, SSA [2, 3, 6, 14] and, subsequently the H_2 production rate. However, the impact of hydrothermal synthesis factors on the 1D TiO_2 photocatalytic H_2 production rate and optimization of the hydrothermal conditions have not been addressed in previous studies.

Photocatalytic production of H_2 and other fuels is affected by phase structure, crystal size, BET SSA, bandgap [15-17], band edge positions [17, 18], charge transfer [19], material stability [20, 21], cocatalyst [22-25], availability [26], complementary metal oxide semiconductor [27, 28] and toxicity [26]. Substrates such as water [19, 29] and ethanol [24] have been used to produce H_2 using photocatalysts. Other electron donors (ED) employed to produce H_2 utilizing TiO_2 under UV light conditions include methanol, 1,2,3 propanetriol and glucose [30].

After absorbing photons, photocatalysts generates and separates electrons (e^-) and holes (h^+). Next, the photogenerated electrons reduce H^+ to generate H_2. The water splitting reaction is described in the following half-cell reactions:

$$2H^+ + 2e^- \rightarrow H_2 \ (photocathode)\ [26] \quad (1)$$

$$H_2O + 2h^+ \rightarrow \frac{1}{2}O_2 + 2H^+ \ (photoanode)\ [26] \quad (2)$$

In the presence of sacrificial ED [30, 31] such as ethanol, the photogenerated holes react with the ED and subsequently, the recombination of electrons and holes in photocatalyst are suppressed [30, 31]. This suppression process significantly increases the H_2 production rate as well as photocatalytic stability [30, 31]. The photoanode water splitting half reaction is as follows [24, 32]:

$$CH_3CH_2OH + 2h^+ \rightarrow 2H^+ + CH_3CHO \ (photoanode)\ [24, 32] \quad (3)$$

Ethanol, a renewable fuel produced mainly from corn, with a specific heating value of approximately 29.7 $MJ \cdot kg^{-1}$ is less when compared to H_2 with a specific heating value of approximately 141.8 $MJ \cdot kg^{-1}$ [33]. In addition, the decomposition of ethanol contributes to a high H_2 production rate and quantum efficiency [34]. Hence, H_2 with a larger energy content is preferred when compared to ethanol as a fuel source.

The first objective of this study was to employ an alkaline hydrothermal method to synthesize 1D TiO_2 photocatalysts under variable reaction conditions. The second objective was to employ a three-factor and three-level Box Behnken design (BBD) to evaluate the effects of selected hydrothermal process conditions (reaction temperature, the NaOH concentration and the TiO_2 precursor concentration) on the photocatalytic 1D TiO_2 H_2 production rate. The third objective was to optimize the hydrothermal conditions and synthesize 1D TiO_2 with a maximum H_2 production rate using the BBD model. The final objective was to decorate the optimized BBD

TiO_2 catalyst with Pt and Au noble metals and investigate the photocatalytic H_2 production using ethanol, methanol, formic acid and 1,2,3 propanetriol.

2. Experimental

Commercial TiO_2 nanoparticles (P25) were purchased from Degussa (Evonik Industries, Germany). NaOH (97% purity), ethanol (95% purity), $HAuCl_4$ (99.9% purity), (99.5% purity), methanol (99.8% purity), formic acid (95% purity), 1,2,3 propanetriol (99.5% purity), F-doped SnO_2-coated (FTO) glass, polyethylene glycol (PEG, molecular weight 20 000) and HCl (37 wt%) were purchased from Fischer Scientific (Ontario, Canada).

2.1. Preparation of 1D nanometric TiO_2 photocatalyst

1D TiO_2 samples were prepared using the alkaline hydrothermal route [10, 12]. Briefly, TiO_2 nanoparticles (Aeroxide TiO_2 P25, Evonik Corporation, Parsippany, New Jersey) were added into 70 mL of a NaOH solution. The TiO_2 concentration and the NaOH concentration used in the study are shown in Table 1. The mixture (total volume 70 mL) was poured into a 100-mL Teflon® capped container. The Teflon® container was placed into a stainless-steel bomb, capped then heated at desired temperature for 48 h and subsequently, cooled to room temperature. The resulting product was centrifuged and washed with 0.1 M HCl solution. The white paste was repeatedly washed with deionized water until pH = 7 and calcined at 400°C for 2 h to produce 1D TiO_2 nanomaterials. The hydrothermal conditions for temperature, NaOH concentration and TiO_2 concentration (Table 1) were based on previous research [14].

Table 1: Three selected factors and three level.

Level	Factors		
	Temperature (°C)	NaOH concentration (M)	TiO_2 concentration ($g \cdot L^{-1}$)
-1	120	5	14
0	150	10	43
1	190	15	100

Note: the reaction mixture volume is 70 mL.

2.2. Characterization studies

The 1D TiO_2 photocatalyst morphology was characterized using field emission scanning electron microscopy (FESEM; JEOL, Japan) and high resolution transmission electron microscopy (HRTEM) (300kV, JEOL 3010, Japan). X-ray diffraction (XRD) analysis of the samples was performed using an X-ray diffractometer (Rigaku, MI) equipped with Cu K_∂ radiation source. An Alpha300 RA argon laser Raman spectrometer (WITec, Germany) with an excitation wavelength set at 532 nm was used to conduct the Raman studies. UV-Vis spectra analysis was recorded on a Cary 300 UV-Vis (Agilent Technologies, Santa Clara, CA). A Micromeritics ASAP 2020 Brunauer–Emmett–Teller (BET) analyzer (Micromeritics Instrument, Norcross, GA) was used to obtain nitrogen adsorption–desorption isotherms at 77K. The BET SSA for each sample is provided in Table 2.

Table 2: Design matrix for experimental factors and response (H_2 production rate, mean crystal size and BET SSA) at different factor levels.

	Factors[a]			Response		
Expt. #	T (°C) (X_1)	NaOH (M) (X_2)	TiO_2 (g·L^{-1}) (X_3)	H_2 production rate (μmol·h^{-1})	Mean crystal size L (nm)	BET SSA (m^2·g^{-1})
1	120	5	43	193±7	9. 5±0.1	182 ± 5
2	190	5	43	298±10	21.5±0.2	125 ± 5
3	120	15	43	463±14	19.9±0.1	138 ± 3
4	190	15	43	72±4	57.2±0.4	37 ± 3
5	120	10	14	271±8	18.2±0.1	146 ± 5
6	190	10	14	95±4	46.4±0.3	73 ± 3
7	120	10	100	224±8	17.6±0.2	149 ± 5
8	190	10	100	103±5	48.2±0.3	39 ± 3
9	150	5	14	204±8	16.9±0.2	174 ± 5
10	150	15	14	284±10	58.3±0.3	61 ± 3
11	150	5	100	395±13	21.2±0.2	140 ± 4
12	150	15	100	283±10	18.8±0.2	137 ± 5
13	150	10	43	393±13	19.5±0.2	151 ± 4
14	150	10	43	389±12	19.8±0.2	152 ± 5
15	150	10	43	383±8	20.5±0.2	148± 5

Note: [a] T, NaOH and TiO_2 represent temperature, NaOH and TiO_2 concentration. [b] the reaction mixture volume is 70 mL.

141

142 *2.3. Photocatalytic hydrogen production*

143 Photocatalytic experiments were conducted using quartz tubes (25 mm ID × 250 mm length)
144 (Technical Glass Products Inc., Painesville, OH) sealed with aluminum crimp caps and Teflon®
145 lined rubber septa. All reaction conditions were examined in triplicate conditions. The sealed
146 photocatalytic reaction tubes were irradiated with a 300-nm UV light source (LZC-UVB-016
147 lamp, Luzchem, ON, Canada) as described in a previous study by Ray *et al.* [35] . The average
148 intensity of UV irradiance was 9 mW·cm^{-2}. The reaction mixture was stirred to maintain the
149 photocatalyst in suspension, minimize particle agglomeration and mass transfer limitation. The
150 reactor temperature was maintained at 37±2°C.

The 50-mL reaction mixture contains 0.2 g·L^{-1} of the photocatalyst and 20% (v/v) ethanol as ED. The reaction mixture was purged with nitrogen (N_2) gas to remove oxygen. Next, the reaction mixture was ultrasonicated and magnetically stirred under dark condition for 1 h before initiation with UV light. Next, the reaction mixture was exposed to UV light and maintained at 37±2°C. At specific time intervals, headspace samples were collected and the H_2 concentration was determined using a gas chromatograph (GC) (Varian CP-3800). The GC was configured with a 2 m long x 2 mm I.D. Carbon Shin Column (Alltech, Deerfield, IL) and a thermal conductivity detector (TCD) at 200°C. The oven and injector temperatures were set at 200°C and 150°C, respectively. Nitrogen gas was used as a carrier gas at a flowrate of 15 mL·min^{-1}. The GC detection limit was approximately 310 umol·L^{-1} for H_2. The photocatalyst reaction mixture was irradiated for 5 h using a 300-nm monochromatic UV light source. The irradiation area for reaction mixture in each tube was 58 cm^2. The H_2 production rate (μmol·h^{-1}) for each sample is shown in Table 2.

The quantum efficiency (ε) was calculated using Eq. (4) and (5) [36].

$$N = \frac{E\lambda}{hc} = \frac{9\times10^{-3}\times58\times3600\times300\times10^{-9}}{6.626\times10^{-34}\times3\times10^{8}} = 2.83\times10^{21} \quad (4)$$

$$\varepsilon = \frac{2\times the\ number\ of\ evolved\ hydrogen\ molecules}{the\ number\ of\ incident\ photons}\times 100\%$$

$$= \frac{2\times6.02\times10^{23}\times H_2\ production\ rate\ \times1h}{2.83\times10^{21}}\times 100\% \quad (5)$$

Where N is the photon number in 1 h; E is the energy rate of incident photons; λ is the wavelength in nm; h is Planck's constant; and c is the photon velocity. Additional photocatalytic H_2 production experiments were conducted using solar irradiation (310-800 nm) (LZC-VIS-016,

Luzchem, ON, Canada) with average intensity of 2 $mW \cdot cm^{-2}$. Other EDs examined in the study included 20% (v/v) methanol, 20% (v/v) formic acid and 20% (v/v) 1,2,3 propanetriol.

2.4. *Optimization study*

The experimental design was based on a 3-factor and 3-level Box-Behnken design (BBD) [37]. The experimental design was used to optimize key process factors (Table 1) to improve the H_2 production rate with using ethanol as the ED. A total of 15 experimental points (#1 to #15) were conducted with each condition under triplicate (Table 2). Experiments, designated as #13, #14 and #15, were conducted as central points to evaluate the magnitude of the error in the study. The experimental factors and H_2 production rate (Y) (response variable) were modeled using Minitab 15 (Minitab Inc., State College, PA) to fit a full quadratic equation (Eq. (6)):

$$Y = a_0 + \sum_{i=1}^{3} a_i X_i + \sum_{i=1}^{3} a_{ii} X_i^2 + \sum_{i=1}^{3} \sum_{i<j=2}^{3} a_{ij} X_i X_j \quad (6)$$

where X_i's are input variables which influence the response variable Y, a_o is an offset term, a_i is the i^{th} linear coefficient, a_{ii} is the quadratic coefficient, and a_{ij} is the ij^{th} interaction coefficient. The X_1, X_2 and X_3 represent the synthesis temperature, NaOH concentration and TiO_2 concentration, respectively (Table 2).

The quadratic model was employed to predict reaction conditions which produced 1D TiO_2 with a maximum H_2 production rate. A D-optimality analysis [38] was performed to find optimal conditions for the three factors under consideration (maximize the H_2 production rate). The coefficient values for fitting the full quadratic model were determined using the H_2 production rate and a multiple regression analysis. An analysis of variance (ANOVA) was

conducted using the observed responses for samples #1 to #15) (Table 2). Only significant terms with p values < 0.05 were included into the model. A normal distribution plot together with the Anderson-Darling (AD) [35] test was used to determine the adequacy of the model.

2.5. TiO_2 photocatalyst decorated with Au and Pt nanoparticles

The TiO_2 photocatalyst sample was decorated with Au nanoparticles based on work by Pu et al. [39]. 1D TiO_2 (500 mg of optimized 1D TiO_2 synthesized at 126°C, 15 M NaOH and 49 $g \cdot L^{-1}$ TiO_2) was first dispersed in the reaction mixture consisting of 500 mL deionized water and 250 mL ethanol followed by the addition of 10 mL of 0.1 M NaOH solution. The mixture was heated to 50°C, followed by addition of 6 mL of a 5 mM $HAuCl_4$ solution. Ethanol was used as a reducing agent to facilitate Au growth. The mixed solution was maintained at 50°C for 3 h with vigorous stirring. The product (Au-decorated 1D TiO_2 with the Au content of 2 wt%) was filtered, washed with deionized water and ethanol, and then dried at 60°C in air for 12 h. For the Pt-decorated 1D TiO_2 with a Pt content of 2 wt%, a similar procedure was employed with using H_2PtCl_6 as Pt source and UV light was used to assist in the reduction of H_2PtCl_6 to Pt.

3. Results and discussion

3.1. 1D TiO_2 morphology

Field emission scanning electron microscopy (FESEM) and high resolution transmission electron microscopy (HRTEM) images for selected 1D TiO_2 samples are shown in Figure 1. 1D structures (nanorods and nanowires) with large differences in the diameter and length were characteristic of TiO_2 synthesized under different reaction conditions. Nanorods morphology with lengths ranging from 20 nm to 100 nm and the diameter of approximately 10 nm were

observed in the sample (#1) (Figure 1a) synthesized at 120°C and with 5 M NaOH plus 43 g·L^{-1} TiO_2 (Figure 1e). Lattice fringes observed with 0.35 nm spacing (Figure 1e) indicate the presence of anatase in the 1D TiO_2 structure (sample #1) [40]. Increasing reaction temperatures and NaOH concentrations caused increasing length, increasing diameter and phase structure changes. Nanowire morphology with lengths reaching 3 μm and diameter ranging from 10 nm to 100 nm was observed for sample #4 (synthesized at 190°C, 15 M and 43 g·L^{-1}) (Figure 1b). The FESEM image for sample #8 (190°C, 10 M and 100 g L^{-1}) (Figure 1c) indicates nanowires with lengths in the micrometer range. The wide distribution of diameter for sample #8 was variable from 10 nm to hundreds of nanometers. The lattice fringes of with 0.62 nm spacing (Figure 1f) indicate the TiO_2 nanowire (sample #8) consisted of the TiO_2-B phase [41]. The FESEM image for sample #9 (150°C, 5 M and 14 g L^{-1}) (Figure 1d) indicate nanowires with lengths in the hundreds of nanometers range. Lowering the temperature as well as lower NaOH concentration levels were linked to smaller diameter and decreasing crystal size (sample #1). In comparison, higher temperatures and NaOH concentrations were associated with larger diameter (Sample # 6 and 8), increasing length (sample #9) and increasing crystal size. The FESEM images provided evidence showing the hydrothermal synthesis factors significantly impacted the 1D TiO_2 diameter and crystal size. The formation of 1D TiO_2 nanostructures was controlled by shearing, exfoliation, delamination of lamellar nanosheets and scrolling lamellar nanosheets into 1D structure [42, 43].

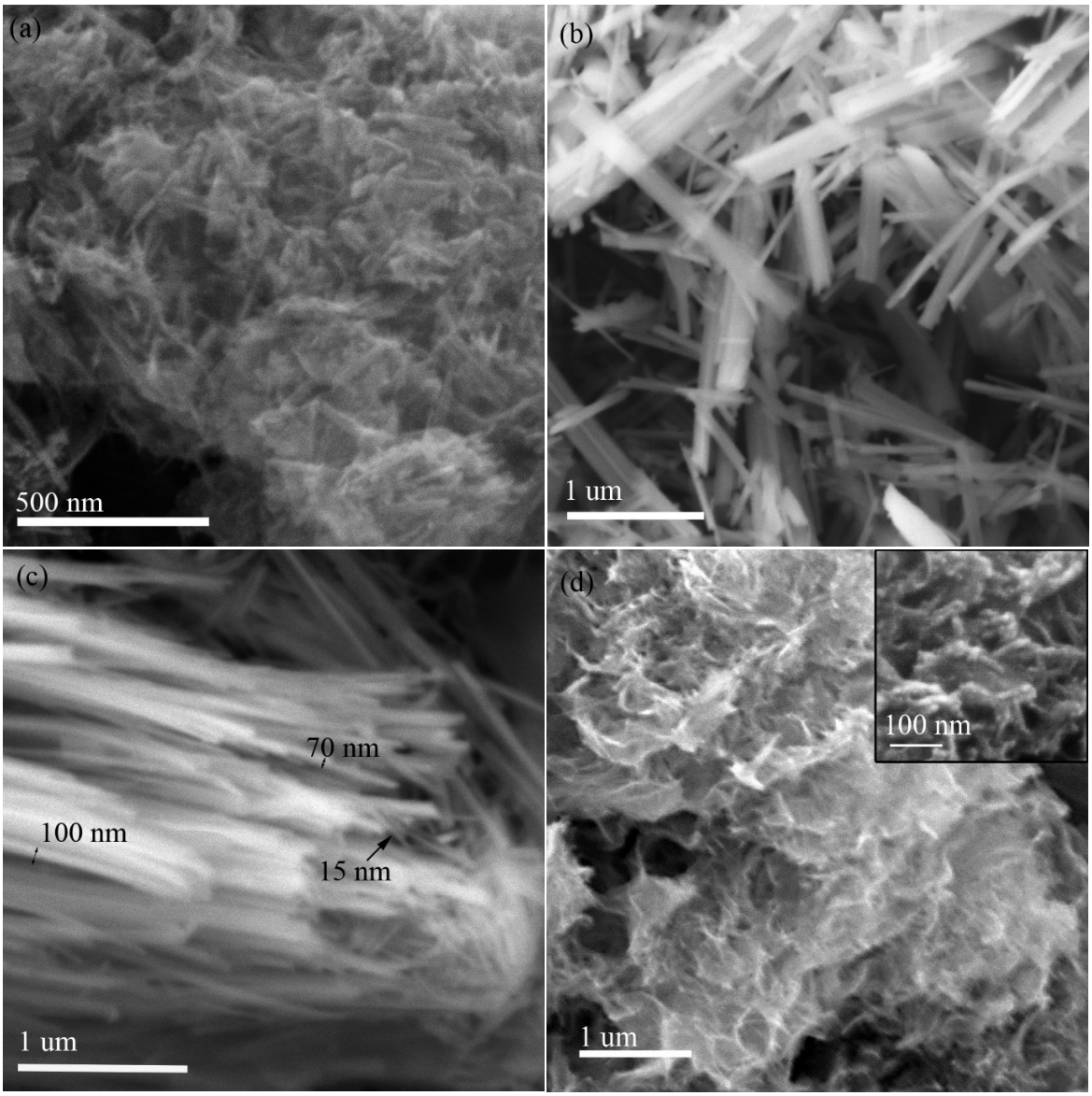
(a)
500 nm
(b)
1 um
(c)
70 nm
100 nm
15 nm
1 um
(d)
100 nm
1 um

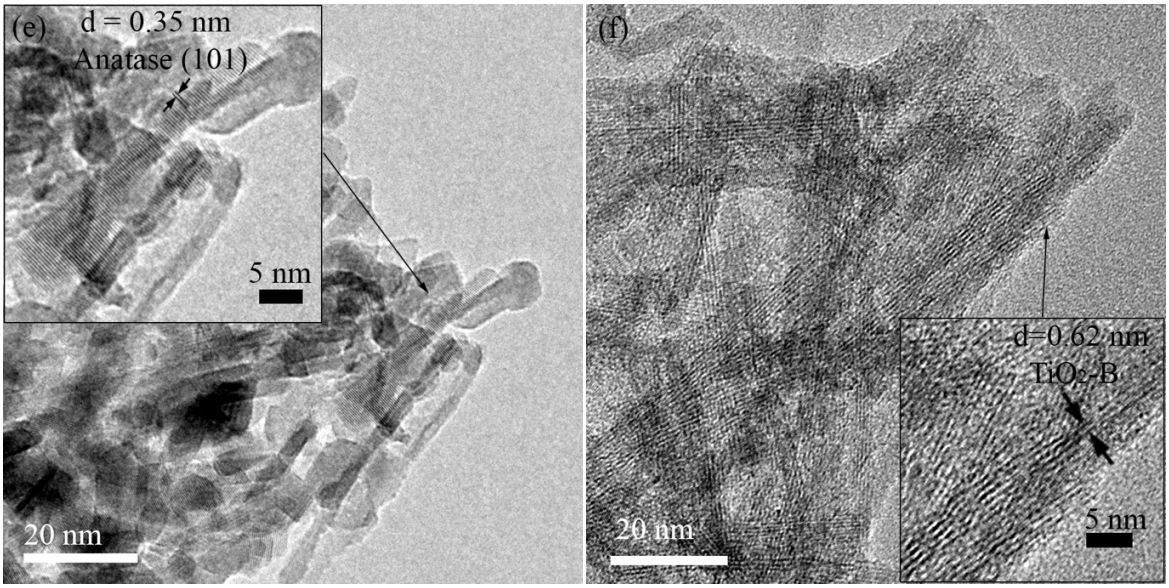

Figure 1: 1D TiO_2 field emission scanning electron microscopy (FESEM) and high resolution transmission electron microscopy (HRTEM) images (a) FESEM image for sample #1 synthesized at 120°C, 5 M NaOH and 43 $g \cdot L^{-1}$; (b) FESEM image for sample #4 synthesized at 190°C, 15 M NaOH and 43 $g \cdot L^{-1}$; (c) FESEM image for sample #8 synthesized at 190°C, 10 M and 100 $g \cdot L^{-1}$; (d). FESEM image for sample #9 synthesized at 150°C, 5 M NaOH and 14 $g \cdot L^{-1}$; (e) HRTEM image sample #1 synthesized at 120°C, 5 M NaOH and 43 $g \cdot L^{-1}$ and (f) HRTEM image for sample #8 synthesized at 190°C, 10 M and 100 $g \cdot L^{-1}$.

3.2. Photocatalytic hydrogen production

Significant differences in H_2 production were observed for 1D TiO_2 samples prepared using different reaction conditions. Hydrogen production versus time profiles are shown in Figure 2a for BBD sample #3 plus the P25 control. Control experiments were conducted employing with and without P25 nanoparticles. The mean H_2 production rate (Y value) was 0 $\mu mol \cdot h^{-1}$ without a photocatalyst; however, with the addition of P25 nanoparticles, the mean production rate increased to 235±8 $\mu mol \cdot h^{-1}$. In comparison, the production rate of 463±14 $\mu mol \cdot h^{-1}$ ($\varepsilon = 19.3 \pm 0.6\%$) for sample #3 (synthesized at 120°C, 15 M NaOH and 43 $g \cdot L^{-1}$ TiO_2) was approximately 2-fold larger than P25 ($\varepsilon = 10.0 \pm 0.4\%$) using ethanol as an ED. Notice sample #3 was characteristic with nanorods structure of approximately 10 nm diameter (Figure 2b). The

ε value for the Pt-TiO_2 catalyst was 5-fold greater than the ε value for TiO_2 when employing pure water as a substrate under UV light conditions . The photocatalytic H_2 production rate showed an approximate 110-fold increase using 20 v/v% ethanol as an ED when compared to using water (Figure S1). The H_2 production rates are listed in Table 2. The effect of ethanol concentration on H_2 production rate was evaluated (Figure S1). For various ethanol concentrations tested, the highest H_2 production rate was observed when using a 20 v/v% aqueous ethanol solution.

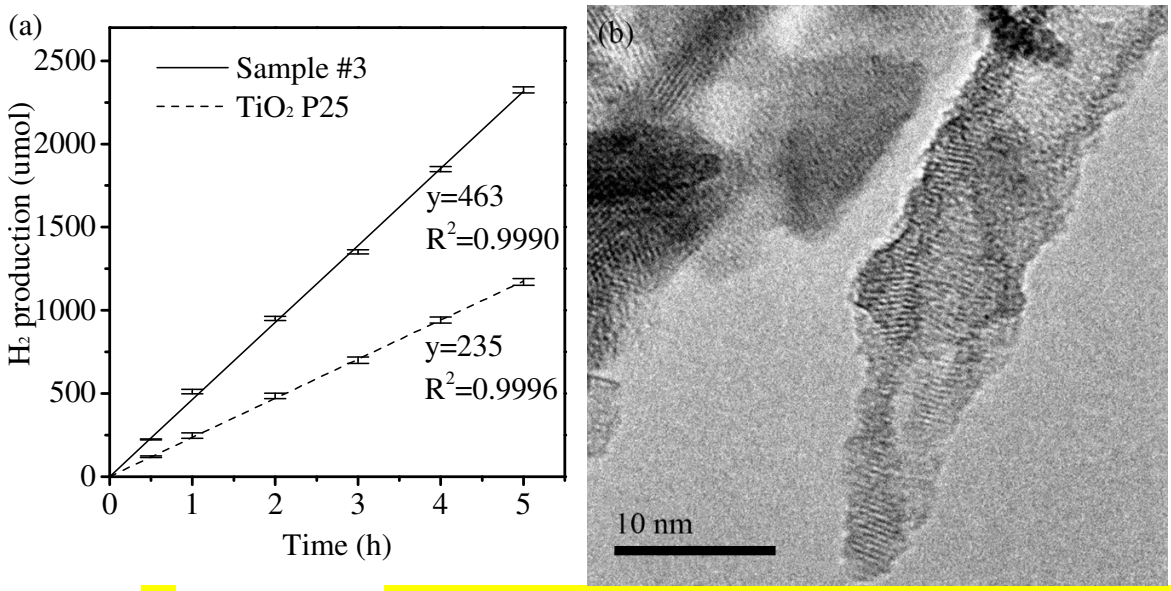

Figure 2: (a) H_2 production (b) High resolution transmission electron microscopy (HRTEM) image for sample #3 and TiO_2 precursor using 300-nm UV light.

3.3. Modeling and effects of factors on the H_2 production rate (response variable) for ethanol

For the response surface optimization study, three sets (replicates) of 15 experiments were conducted to compute the H_2 production rate under 15 conditions (Table 2). A multiple regression analysis was used to develop a full quadratic equation (7) which describes the H_2 production rate, Y, as a function of the hydrothermal process conditions.

$$Y = -2964 + 34.28X_1 + 124.34X_2 + 8.55X_3 - 0.7X_1X_2 + 0.006X_1X_3 - 0.239X_2X_3 - 0.096X_1^2 - 0.269X_2^2 - 0.058X_3^2 \quad (7)$$

where Y is the H_2 production rate ($\mu mol \cdot h^{-1}$), X_1, X_2 and X_3 represent the reaction temperature (^oC), NaOH concentration (M) and TiO_2 concentration ($g \cdot L^{-1}$), respectively.

The relationship between the synthesis factors, phase structure and the H_2 production rate is shown in the 3D surface plots and the corresponding contour plots (Figure 3). Interaction between the temperature and the NaOH concentration (Figures 3a and b) suggests that both parameters significantly affected the 1D TiO_2 phase structure and the H_2 production rate (Figure S2). A relatively low temperature at 120^{o}C and a high NaOH concentration at 15 M were closely associated with producing a pure anatase catalyst with a high H_2 production rate. Increasing temperatures or decreasing NaOH concentrations were correlated with decreasing H_2 production rates. The biphasic anatase-rutile structure, synthesized at 120^{o}C and 5 M NaOH, was linked to a lower H_2 production rate. In addition, a significant decrease in the H_2 production rate was observed for the biphasic anatase-TiO_2-B structure which was synthesized at 190^{o}C and with ≥10 M NaOH. These observations indicate the rutile and TiO_2-B phases are closely correlated with decreasing photocatalytic H_2 production. Interaction between temperature and TiO_2 concentration (Figure 3c and d) and interaction between NaOH concentration and TiO_2 concentration (Figure 3e and f) confirmed decreasing the synthesis temperature and increasing the NaOH concentration were closely associated with increasing the H_2 production rate. In addition, the surface and contour plots indicate the optimum H_2 production rate was obtained with a TiO_2 concentration of approximately 50 $g \cdot L^{-1}$.

364 The D-optimality index was used to locate the maximum response (Y) region within the
365 factor space under consideration (Figure S3). A maximum response of 470 µmol·h^{-1} was
366 predicted for 1D TiO_2 synthesized at 126ºC, 15 M NaOH and 49 g·L^{-1} TiO_2. Additional
367 experiments were conducted to verify the maximum response when using the 1D TiO_2
368 photocatalyst under the predicted conditions. The predicted value was slightly underestimated
369 when compared to the observed response of 475±12 µmol·h^{-1} (ε=20.2±0.5%). Recall, pure
370 anatase with a mean crystal size of 20.1±0.2 nm and BET SSA of 140±3 m^2·g^{-1} was observed for
371 1D TiO_2 synthesized under optimum conditions. The opitimum H_2 production rate value was
372 approximately 2-fold larger when compared to commercial P25 when employing a 20 v/v%
373 ethanol feed. This H_2 production rate was significantly improved when compared to reported
374 production rates of 348 µmol·h^{-1} for biphasic anatase-TiO_2-B [10]. The optimum H_2 production
375 rate of 470 µmol·h^{-1} for the optimized 1D TiO_2 was normalized to a mass basis. The specific H_2
376 production rate (per g of photocatalyst) attained was 23,500 µmol·h^{-1}·g^{-1}. The maxmum specific
377 H_2 production rate was significantly enhanced when compared to data reported for pure anatase,
378 pure rutile, flame spray pyrolysis-synthesised TiO_2 and Au/TiO_2 [44].
379

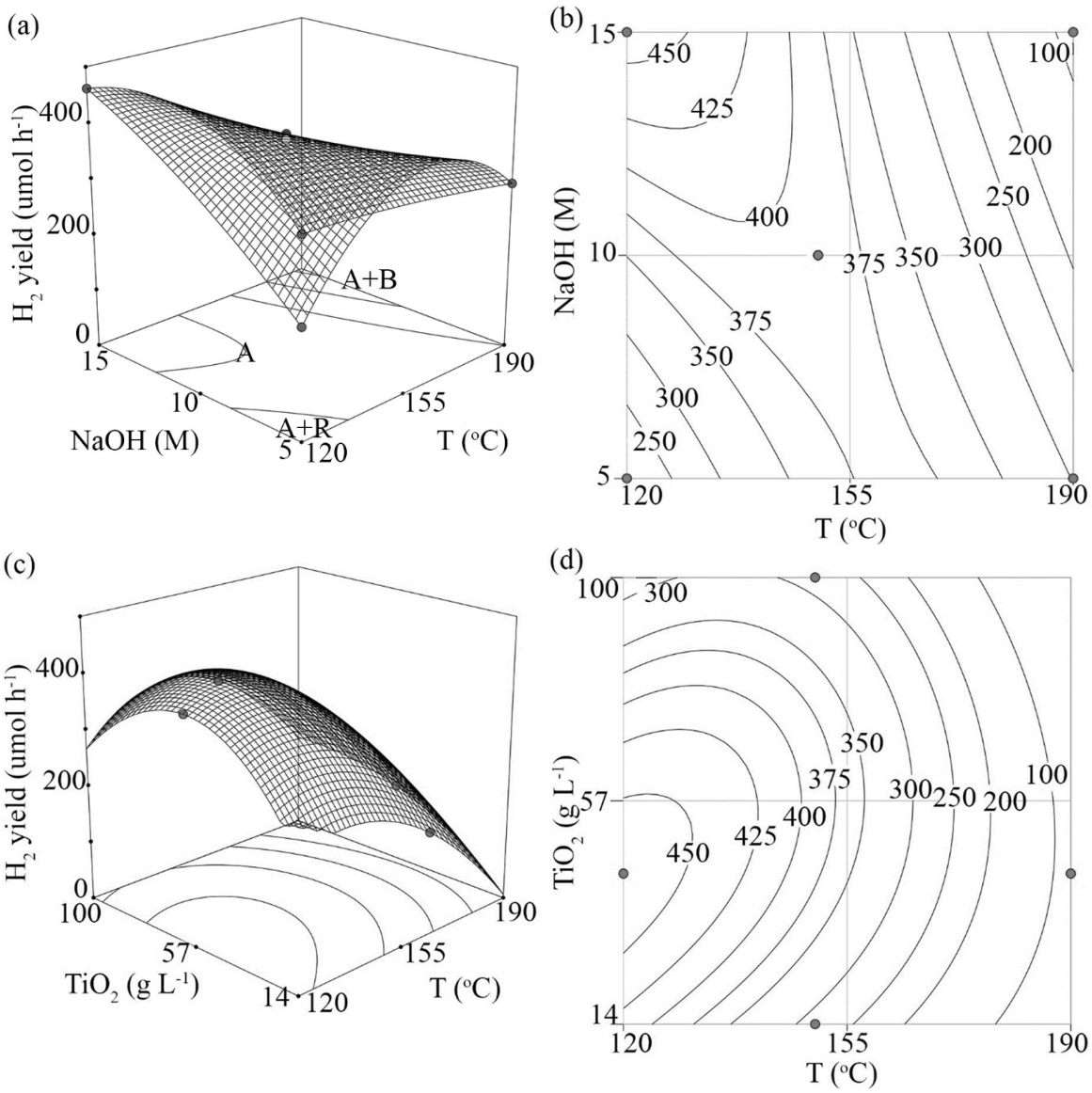
(a)
H2 yield (umol h-1)
400
200
0
A
A+B
A+R
15
10
5
NaOH (M)
120
155
190
T (°C)
(b)
NaOH (M)
15
10
5
450
425
400
375
350
300
250
200
100
120
155
190
T (°C)
(c)
H2 yield (umol h-1)
400
200
0
100
57
14
TiO2 (g L-1)
120
155
190
T (°C)
(d)
TiO2 (g L-1)
100
57
14
300
350
375
400
425
450
300
250
200
100
120
155
190
T (°C)

380

381

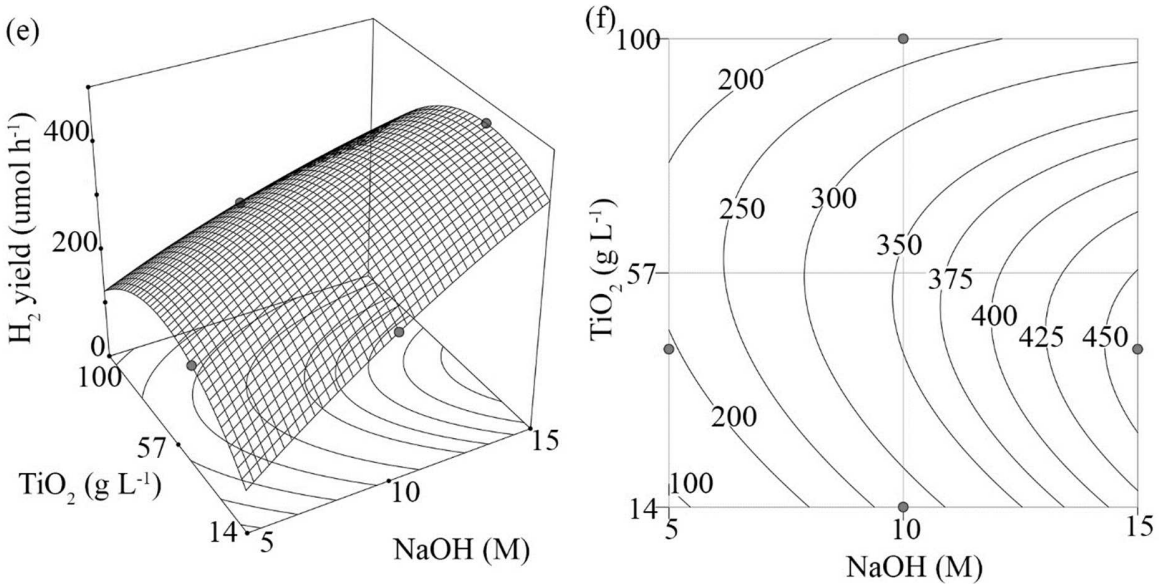

Figure 3: 3D response surface and contour plots for: (a) and (b) Interaction between hydrothermal temperature and NaOH concentration set at 43 g·L^{-1} TiO_2, (c) and (d) Interaction between hydrothermal temperature and TiO_2 concentration set at 15 M NaOH concentration, (e) and (f) Interaction between NaOH concentration and TiO_2 concentration set at 120ºC temperature.

Note: A, R and B represents the anatase, rutile and TiO_2-B phases, respectively.

3.4. Response surface model development

An analysis of variance (ANOVA) (Table S1) of the model full quadratic equation (7) was employed to determine the significance and adequacy of the model. The quadratic model with an overall p-value ≤ 0.05 [37, 38, 45, 46] and a F-value ≤ to the critical value (2.01 at 5% level of significance) [37, 38, 45, 46] indicate the model was statistically significant. However, two variables (X_2^2 and X_1X_3) with p-value ≥ 0.05 were statistically insignificant with no individual effect on the full quadratic model. These terms were deleted from model using a backward elimination method [38]. The revised response surface model is designated as equation (8):

$$Y = -2974 + 34.43X_1 + 118.96X_2 + 9.40X_3 - 0.7X_1X_2 - 0.239X_2X_3 - 0.095X_1^2 - 0.058X_3^2 \quad (8)$$

where Y is the H_2 production rate ($\mu mol \cdot h^{-1}$), X_1, X_2 and X_3 represent temperature (^oC), NaOH concentration (M) and TiO_2 concentration ($g \cdot L^{-1}$), respectively.

3.5. Response surface model verification

A scatter plot comparing the experimental and the model predicted values (Figure 4a) indicate a reasonable correlation at each level. The Anderson-Darling (AD) statistic (Figure 4b) was employed to assess the adequacy of fitting the model to the experimental data by determining the normal distribution of the residuals (difference between the predicted and experimental values) [47]. An AD value of 0.379 (≤ the critical value of 0.735 for 45 samples and at a 5% level of significance) [47] and a p-value of 0.391 (≥ 0.05) suggest the model's predicted valued correlated with the experimental values.

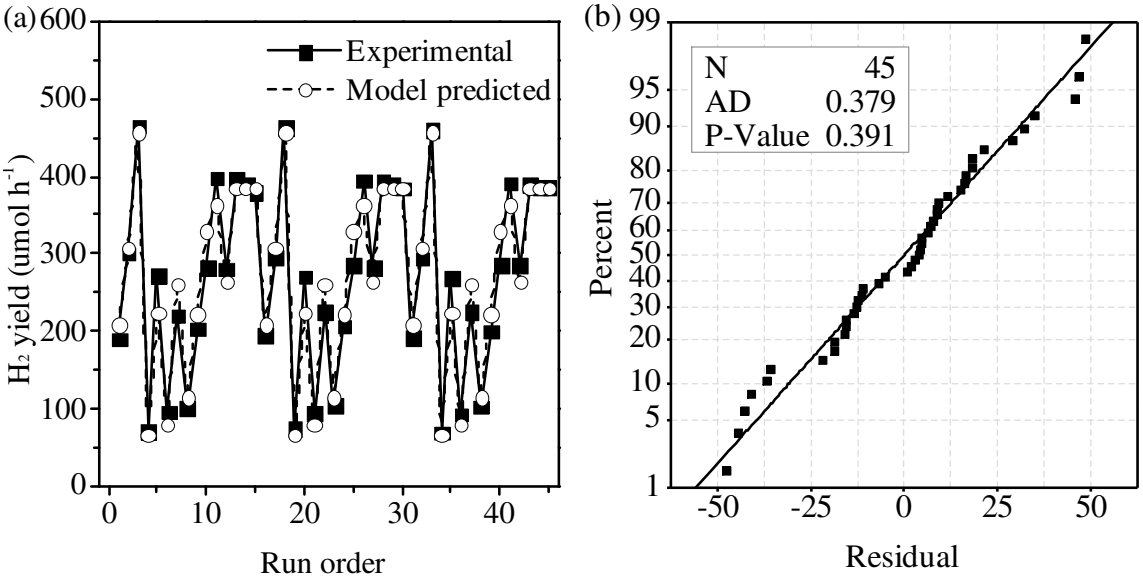

Figure 4: Accuracy evaluation of the response surface model. (a) Scatter plot of the H_2 produciton rate ($\mu mol \cdot h^{-1}$) versus experiment order (45 experiments). (b) Anderson-Darling normality plot of residuals.
Notes: N = the number of experiments conducted in this study; P-Value = level of confidence; AD = Anderson-Darling statistic.

Validation of the model accuracy was examined by varying a single factor in three additional experiments (Figure 5). The model predicted trend was comparable to the experimental trend for varying each factor. For a temperature range from 120 to 190°C (Figure 5a), the model predicted values were close to the experimental values with a slight overestimate at each temperature level. For the NaOH concentration (Figure 5b), the predicted values were in agreement with the experimental data with a slight overestimate at 5 M NaOH. For the TiO_2 concentration, the model predicted values which were reasonably close to the observed values for each level of TiO_2 concentration with a slight underestimate at 100 $g \cdot L^{-1}$ TiO_2 and a slight overestimate at 14 and 43 $g \cdot L^{-1}$ (Figure 5c). Additional experiments (Table S2) were conducted to compare the model predicted value and experimental value. The results indicate the model's predicted values correlated with the experimental values.

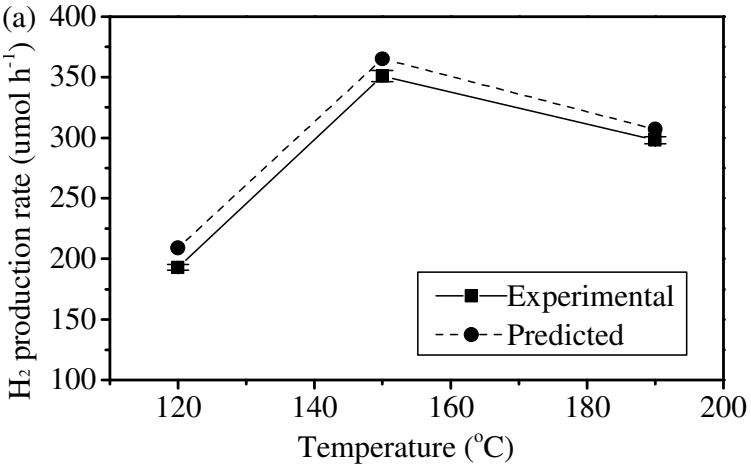

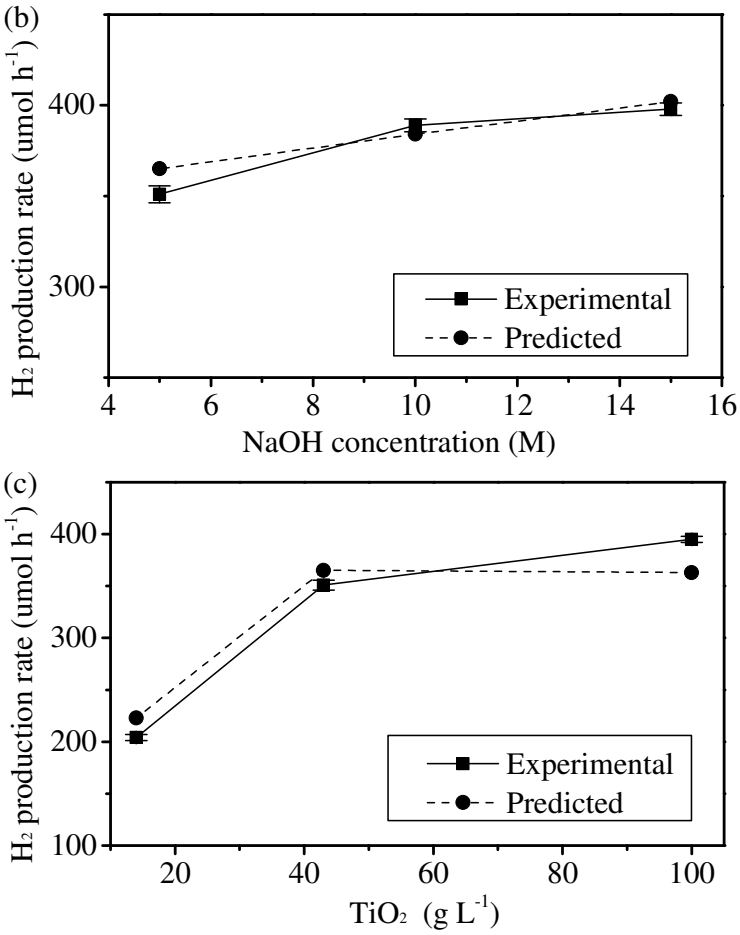

Figure 5: Validation study of the response surface model for the varied factors under consideration. (a) H_2 production rate versus temperature at experimental conditions set at 5 M NaOH and 43 g·L^{-1} TiO_2; (b) H_2 production rate value versus NaOH concentration at experimental conditions set at 150°C and 43 g·L^{-1} TiO_2; (c) H_2 production rate versus TiO_2 concentration at experimental conditions set at 150°C and 5 M NaOH.

3.6. Phase structure, crystal size and bandgap energies

XRD analysis and diffuse reflectance UV-Vis spectroscopy were used to evaluate the phase structure, crystal size and bandgap energy for the BBD samples. The XRD patterns for selected BBD samples #1, #3 and #8 are shown in Figure 6a and the phase structure is summarized in Table 3 for all the samples. The three phase structures observed in this study included pure anatase [48], biphasic anatase-rutile [49-51] and the biphasic anatase-TiO_2-B [10] structures (Figure 6a). The biphasic anatase-rutile structure, similar to that in P25, was only detected in

449 sample #1 [49-51] (Figure S4), while pure anatase phase and the biphasic anatase-TiO_2-B
450 structures were observed in a majority of the samples. The mean crystal sizes (L, nm) for sample
451 #1-15 (Table 2) were calculated using the Scherrer equation (equation 9) and XRD data.

452 $$L=K\lambda/\beta.\cos\theta \text{ [52]} \quad (9)$$

453 where K, λ and β represent the shape factor (0.89), the wavelength of XRD radiation (0.154 nm)
454 and the half maximum of a full peak, respectively.

455

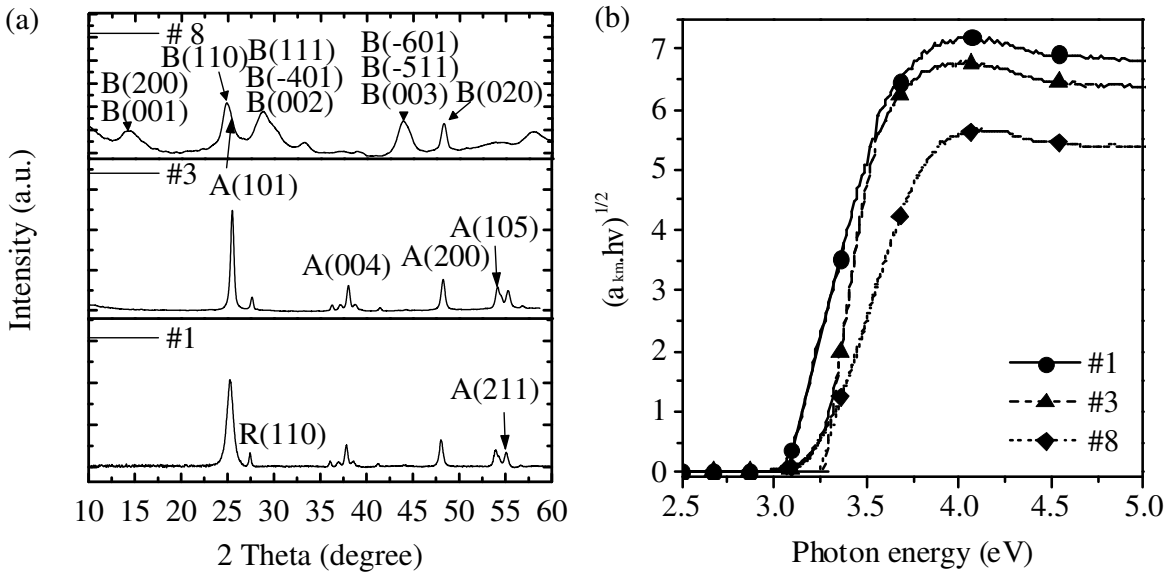

456
457 Figure 6: X-ray diffraction (XRD) patterns and $\alpha_{km}hv)^{1/2}$ versus absorbed energy for samples #1,
458 #3, and #8: (a) XRD spectra and (b) $\alpha_{km}hv)^{1/2}$ versus absorbed energy profiles.
459 Notes: [a]. Synthesis parameter details are listed in Table 2; [b]. A(101) peak is positioned on the
460 shoulder and 3. A, R and B represents the anatase, rutile and TiO_2-B phases, respectively.
461

462

463

464

465

466

Table 3. Phase structures, bandgap energies, mean crystal size, BET SSA and H_2 production rate for all BBD samples.

Phase	Sample #	Bandgap energy (eV)	Mean crystal size (nm)	BET SSA ($m^2 \cdot g^{-1}$)	H_2 production rate (μmol·h-1)
Anatase and rutile	1	3.067±0.006	9.5±0.1	182±5	193±7
Anatase	2, 3, 5, 7, 9, 10, 11, 12, 13, 14 and 15	3.258±0.003 to 3.298±0.005	16.9±0.2 to 57.2±0.4	61±3 to 174±5	204±8 to 463±14
Anatase and TiO_2-B	4, 6, 8	3.210±0.007 to 3.229±0.009	46.4±0.3 to 58.3±0.3	37±3 to 73±3	72±4 to 103±5

Note: Sample order number is defined in Table 2.

Diffuse reflectance UV-Vis spectroscopic profiles for selected BBD samples are shown in Figure S5. All the BBD samples with an optical absorption below 400 nm was likely caused by their band-band electron transition [49, 53]. The diffuse reflectance spectra was transformed into corresponding absorption spectra (Figure 6b) using Kubelka-Munk function [54]. The bandgap energy is closely correlated with the phase structure and chemical composition (Table 3). The pure anatase (e.g. sample #3) phase was observed with a large bandgap energy ranging from 3.258±0.003 to 3.298±0.005 eV [55, 56], while the biphasic structure anatase-rutile (sample #1) and anatase-TiO_2-B (samples #4, #6 and #8) showed decreasing bandgap energies of 3.067±0.006 and values ranging from 3.210±0.007 to 3.229±0.009 eV, respectively. In the Ti2p XPS spectra for sample #1 and the optimized 1D TiO_2 (Figure S6) sample, the two main peaks at 458.9 eV ($Ti2p_{3/2}$) and 464.5 eV ($Ti2p_{1/2}$) indicate the presence of Ti^{4+}. In comparison, the deconvoluted peaks located at 457.4 eV ($Ti2p_{3/2}$) and 463.0 eV ($Ti2p_{1/2}$) were due to the presence

of Ti^{3+}. The low peak intensity attributed to Ti^{3+} indicate sample #1 and the optimized 1D TiO_2 contained a small amount of Ti^{3+} and oxygen vacancy.

3.7. The effect on phase structure and crystal size

The H_2 production rates, crystal size and BET SSA are summarized in Table 3 for the BBD 1D TiO_2 samples synthesized under different reaction conditions. Depending on the hydrothermal synthesis conditions, the H_2 production rates was variable from 72±4 to 475±12 $\mu mol \cdot h^{-1}$. The 1D TiO_2 phase structures marked in the 3D response surface plot (Figure 3a) shows the effect of reaction temperature and NaOH concentration on the phase structure and H_2 production rate. The low NaOH concentration (5 M) and reaction temperature (120°C) were correlated with the biphasic anatase-rutile structure. Increasing NaOH concentration and reaction temperature were related to converting rutile into anatase. In addition, higher NaOH concentrations greater than 10 M coupled with a temperature at 190°C were associated with the conversion of anatase to TiO_2-B. Variation of the phase structures had a main effect on the H_2 production rate. The pure anatase (sample #2, #3, #5, #7, #9, #11-15 and the optimized sample synthesized at 126°C, 15 M NaOH and 49 $g \cdot L^{-1}$ TiO_2) were closely linked with increasing the H_2 production rate, while the biphasic anatase-rutile (sample #1) and anatase-TiO_2-B structures (sample #4, #6 and #8) were associated with decreasing H_2 production rate. The pure anatase samples were correlated with high bandgaps ranging from 3.258±0.003 to 3.298±0.005 eV. However, the biphasic anatase-rutile sample #1 showed the lowest bandgap of 3.067±0.006 eV. The lowest H_2 production rate was detected for the biphasic anatase-TiO_2-B structure (sample #4, 6 and 8). The biphasic anatase-TiO_2-B samples showed decreased bandgaps ranging from 3.210±0.007 to 3.229±0.009 eV when compared to the pure anatase samples. The I-t curves for

sample #1 (biphasic anatase-rutile), #8 (biphasic anatase-TiO_2-B), optimized 1D TiO_2 (anatase) and P25 with an on-off UV-light irradiation (300 nm) source are shown in Figure S7. The greatest photocurrent density was observed for the optimized 1D TiO_2 containing anatase. This observation suggests the optimized 1D TiO_2 is characterized by an enhanced charge carrier transportation and separation. The photocurrent densities for sample #1 and P25 were comparable to each other. The lowest photocurrent density caused by the fast recombination of electrons and holes was detected for the sample (#8) containing in the TiO_2-B phase.

The H_2 production rate ($\mu mol \cdot h^{-1}$) for the pure anatase phase samples (Figure 7) suggests the greatest H_2 production rate of 475±12 $\mu mol \cdot h^{-1}$ was observed when the mean crystal size was 20.1±0.2 nm with BET SSA of 140±3 $m^2 \cdot g^{-1}$. Smaller crystal size was closely linked to a larger BET SSA for 1D TiO_2 containing anatase. The BET SSA ($m^2 g^{-1}$) as a function of the mean crystal size is shown as equation (Eq. 10).

$$S = 1518 \times L^{-0.7931} \qquad (16 \leq L \leq 56 \text{ and } R^2 = 95.6\%) \qquad (10)$$

Where S ($m^2 g^{-1}$) and L (nm) represent the BET SSA and the mean crystal size, respectively.

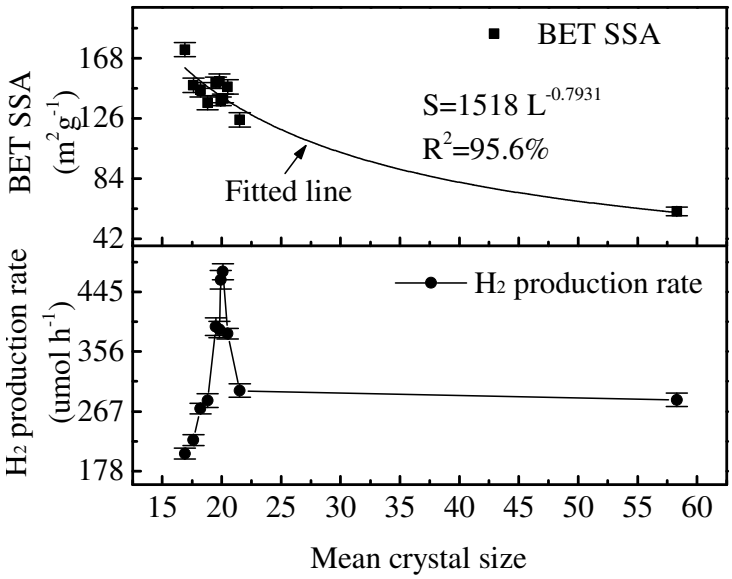

Figure 7: Hydrogen production rate and specific surface area versus anatase mean crystal size. Note: All samples counted in the figure is anatase phase. The L and S represent crystal size and BET SSA, respectively. 16 ⩽L⩽56.

Increasing the H_2 production rate was closely correlated with decreasing the anatase mean crystal size from 58.3±0.3 to 20.1±0.2 nm. The increasing the H_2 production rate was due to increasing the SSA [57] and faster rates of e- and h+ surface reactions with the substrate. The optimum anatase mean crystal size of 20.1±0.2 nm was correlated with a maximum H_2 production rate. However, note the lower H_2 production rate observed below the optimum anatase mean crystal size was caused by fast e^--h^+ recombination [57]. A decreasing H_2 production rate which was correlated with fast e^--h^+ recombination at defective sites on the photocatalyst surface [57]. The significantly great number of defective sites was due to decreasing the crystal size below an optimum value.

3.8. Noble metal decorating and other alcohol sacrificial agents

A significant increase in the H_2 production rate was observed when decorating the TiO_2 photocatalyst with Au or Pt (Figures 8a and b). The catalytic activity of the optimized 1D TiO_2 sample synthesized at 126°C, 15 M NaOH and 49 $g \cdot L^{-1}$ TiO_2 was significantly enhanced by adding Au and Pt (Au/optimum or Pt/optimum) when compared to commercial TiO_2 nanoparticles decorated with Au or Pt (Au/P25 or Pt/P25). The catalytic activity of the optimized 1D TiO_2 samples decorated with 2 wt% Au (Au/optimum) and Pt (Pt/optimum) were 1146±26 $\mu mol \cdot h^{-1}$ (ε = 48.7±1.1%) and 1823±35 $\mu mol \cdot h^{-1}$ (ε = 77.5±1.5%), respectively. These rates were greater than those for other TiO_2 substrates decorated with 2 wt% of each metal. The Pt/optimum 1D TiO_2 activity was greater when compared to the activity for the Au/optimum 1D TiO_2 photocatalyst. The H_2 production rate for Pt/optimum was approximately 5-fold greater when compared to the H_2 production rate (348 $\mu mol \cdot h^{-1}$) for TiO_2 nanotubes decorated with Pt nanoparticles [10].

Photocatalytic H_2 production studies were performed using the Pt/optimized 1D TiO_2 catalyst and different EDs (Figure 8c). The H_2 production rates were 1499±34 $\mu mol \cdot h^{-1}$ (ε = 63.7±1.4%), 1288±37 $\mu mol \cdot h^{-1}$ (ε = 54.8±1.5%) and 710±15 $\mu mol \cdot h^{-1}$ (ε = 30.2±0.6%) for methanol, formic acid and 1,2,3 propanetriol, respectively. In addition, under solar light conditions, the low H_2 production rate for the Pt/optimum 1D TiO_2 photocatalyst of 179±3 $\mu mol \cdot h^{-1}$ (ε = 7.6±0.1%) (Figure 8d) was due to the low irradiation energy and the longer visible light wavelength when compared to only UV light.

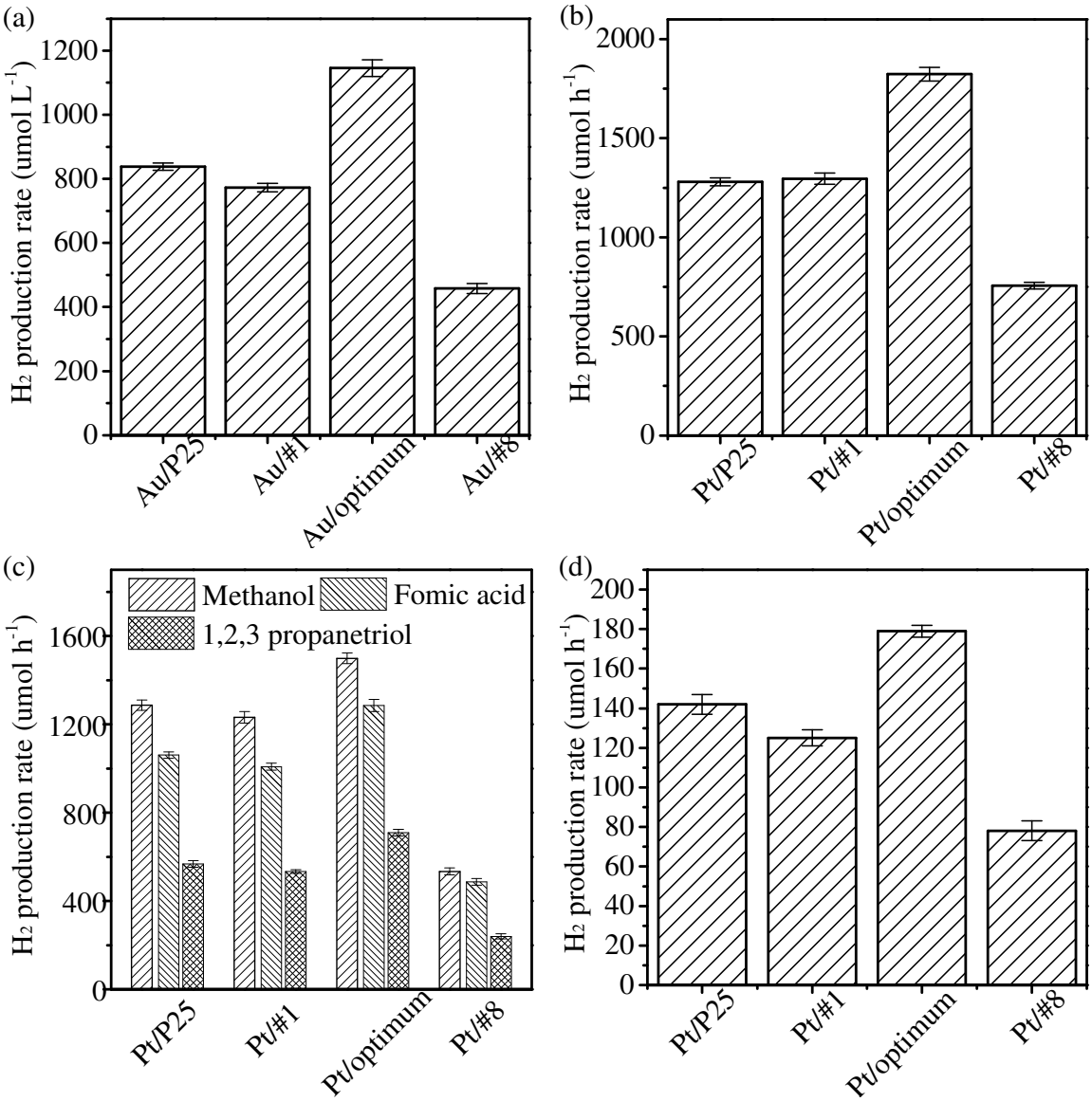

Figure 8: H_2 production rate for (a) TiO_2 decorated with 2% Au under UV light condition, (b) TiO_2 decorated with 2% Pt under UV light condition, (c) Optimized 1D TiO_2 decorated with 2% Pt photocatalysts using methanol, formic acid and 1,2,3 propanetriol under UV light condition, and (d) TiO_2 decorated with 2% Pt using solar simulators.

Note: [a] Au/P25, Au/#1, Au/optimum and Au/#8 represent TiO_2 nanoparticles (P25), sample #1, optimized 1D TiO_2 and sample #8 decorated with 2% Au cocatalysts. [b] Pt/P25, Pt/#1, Pt/optimum and Pt/#8 represent P25, sample #1, optimized 1D TiO_2 and sample #8 decorated with Pt cocatalysts. [c]Optimum. represent optimized 1D TiO_2 synthesized at 126°C, 15 M NaOH and 49 $g \cdot L^{-1}$ TiO_2.

4. Conclusion

1D TiO_2 ranging from nanorods to nanowires were produced using a hydrothermal method with variable reaction conditions. The reaction temperature and NaOH concentration significantly affected the 1D TiO_2 phase structure, crystal size, SSA, bandgap energy and photocatalytic activity. A statistical model evaluated the effects of the hydrothermal synthesis factors on the photocatalytic activity of 1D TiO_2 in terms of the H_2 production rate. The AD and validation test indicated an adequate fit of the statistical model to the experimental data under the conditions examined. The model revealed that a relatively low temperature (126°C) and high NaOH concentration (15 M) were closely linked to producing 1D TiO_2 containing pure anatase. This 1D TiO_2 sample with an optimum mean crystal size was able to maximize the H_2 production rate. The 1D TiO_2 with biphasic anatase-rutile and anatase-TiO_2-B structures was observed with decreasing photocatalytic H_2 production rate. A significant increase in the H_2 production rate was observed for the optimized 1D TiO_2 photocatalysts decorated with Pt or Au. This study demonstrated that 1D TiO_2 containing a controllable phase structure, and crystal size was able to produce a photocatalyst with a H_2 production rate greater than reported values.

5. Acknowledgements

Financial support for this work was provided by the Natural Sciences and Engineering Research Council (NSERC) of Canada (grant # 261797-2009), the Ontario Trillium scholarship program and the University of Windsor (grant #13320).

6. Reference

[1] P. Roy, S. Berger, P. Schmuki, TiO_2 nanotubes: synthesis and applications, Angew. Chem. Int. Ed. 50 (2011) 2904-2939.

[2] D.V. Bavykin, V.N. Parmon, A.A. Lapkin, F.C. Walsh, The effect of hydrothermal conditions on the mesoporous structure of TiO_2 nanotubes, J. Mater. Chem. 14 (2004) 3370-3378.

[3] H.Y. Zhu, Y. Lan, X.P. Gao, S.P. Ringer, Z.F. Zheng, D.Y. Song, J.C. Zhao, Phase transition between nanostructures of titanate and titanium dioxides via simple wet-chemical reactions., J. Am. Chem. Soc. 127 (2005) 6730-6736.

[4] X. Chen, S.S. Mao, Titanium dioxide nanomaterials: Synthesis, properties, modifications, and applications, Chem. Rev. 107 (2007) 2891-2959.

[5] B. Chen, J. Hou, K. Lu, Formation mechanism of TiO_2 nanotubes and their applications in photoelectrochemical water splitting and supercapacitors, Langmuir 29 (2013) 5911-5919.

[6] T. Kasuga, M. Hiramatsu, A. Hoson, T. Sekino, K. Niihara, Formation of titanium oxide nanotube, Langmuir 14 (1998) 3160-3163.

[7] Y. Tang, Y. Zhang, J. Deng, J. Wei, H.L. Tam, B.K. Chandran, Z. Dong, Z. Chen, X. Chen, Mechanical force-driven growth of elongated bending TiO_2-based nanotubular materials for ultrafast rechargeable lithium ion batteries, Adv. Mater. 26 (2014) 6111-6118.

[8] Y.V. Kolen'ko, K.A. Kovnir, A.I. Gavrilov, Hydrothermal synthesis and characterization of nanorods of various titanates and titanium dioxide, J. Phys. Chem. B 110 (2006) 4030-4038.

[9] H.-W. Shim, D.K. Lee, I.S. Cho, K.S. Hong, D.-W. Kim, Facile hydrothermal synthesis of porous TiO_2 nanowire electrodes with high-rate capability for Li ion batteries, Nanotechnology 21 (2010) 255706-255709.

613 [10] H.-L. Kuo, C.-Y. Kuo, C.-H. Liu, J.-H. Chao, C.-H. Lin, A highly active bi-crystalline
614 photocatalyst consisting of TiO_2 (B) nanotube and anatase particle for producing H_2 gas from
615 neat ethanol, Catal. Lett. 113 (2007) 7.
616 [11] A.R. Armstrong, G. Armstrong, J. Canales, P.G. Bruce, TiO_2-B nanowires, Angew. Chem.
617 116 (2004) 2336-2338.
618 [12] A. Kukovecz, K. Kordas, J. Kiss, Z. Konya, Atomic scale characterization and surface
619 chemistry of metal modified titanate nanotubes and nanowires, Surf. Sci. Rep. 71 (2016) 473-
620 546.
621 [13] J. Jitputti, S. Pavasupree, Y. Suzuki, S. Yoshikawa, Synthesis of TiO_2 nanotubes and its
622 photocatalytic activity for H_2 evolution, Jpn. J. Appl. Phys. 47 (2008) 751.
623 [14] **T. Peng**, S. Ray, S.S. Veeravalli, J.A. Lalman, F. Arefi-Khonsari, The role of hydrothermal
624 conditions in determining 1D TiO_2 nanomaterials bandgap energies and crystal phases, Mater.
625 Res. Bull. 105 (2018) 104-113.
626 [15] T. Lavanya, M. Dutta, S. Ramaprabhu, K. Satheesh, Superior photocatalytic performance of
627 graphene wrapped anatase/rutile mixed phase TiO2 nanofibers synthesized by a simple and facile
628 route, J. Environ. Chem. Eng. 5 (2017) 494-503.
629 [16] A.M. Hussein, L. Mahoney, R. Peng, H. Kibombo, C.-M. Wu, R.T. Koodali, R. Shende,
630 Mesoporous coupled ZnO/TiO_2 photocatalyst nanocomposites for hydrogen generation, J.
631 Renew. Sustain. Ener. 5 (2013) 033118.
632 [17] A.L. Linsebigler, G. Lu, J.T. Yates, Photocatalysis on TiO_2 surfaces: Principles,
633 mechanisms, and selected results, Chem. Rev. 95 (1995) 735-758.

634 [18] J. Zhang, Q. Sun, J. Zheng, X. Zhang, Y. Cui, P. Wang, W. Li, Y. Zhu, The characterization
635 of nitrogen doped TiO_2 photoanodes and its application in the dye sensitized solar cells, J.
636 Renew. Sustain. Ener. 3 (2011) 033108.
637 [19] Q. Xiang, B. Cheng, J. Yu, Graphene based photocatalysts for solar fuel generation, Angew.
638 Chem. 127 (2015) 11508-11524.
639 [20] X. Wang, K. Maeda, A. Thomas, K. Takanabe, G. Xin, J.M. Carlsson, K. Domen, M.
640 Antonietti, A metal-free polymeric photocatalyst for hydrogen production from water under
641 visible light, Nat. Mater. 8 (2008) 76-80.
642 [21] S.-W. Cao, Y.-P. Yuan, J. Fang, M.M. Shahjamali, F.Y.C. Boey, J. Barber, S.C.J. Loo, C.
643 Xue, In-situ growth of CdS quantum dots on g-C_3N_4 nanosheets for highly efficient
644 photocatalytic hydrogen generation under visible light irradiation, Int. J. Hydrogen Energ. 38
645 (2013) 1258-1266.
646 [22] M. Nasirian, M. Mehrvar, Modification of TiO_2 to enhance photocatalytic degradation of
647 organics in aqueous solutions, J. Environ. Chem. Eng. 4 (2016) 4072-4082.
648 [23] A. Nada, M. Barakat, H. Hamed, N. Mohamed, T. Veziroglu, Studies on the photocatalytic
649 hydrogen production using suspended modified photocatalysts, Int. J. Hydrogen Energ. 30 (2005)
650 687-691.
651 [24] M. Murdoch, G.I.N. Waterhouse, M.A. Nadeem, J.B. Metson, M.A. Keane, R.F. Howe, J.
652 Llorca, H. Idriss, The effect of gold loading and particle size on photocatalytic hydrogen
653 production from ethanol over Au/TiO_2 nanoparticles, Nat. Chem. 3 (2011) 489-492.
654 [25] K. Connelly, A.K. Wahab, H. Idriss, Photoreaction of Au/TiO_2 for hydrogen production
655 from renewables: a review on the synergistic effect between anatase and rutile phases of TiO_2,
656 Mater. Renew. Sustain. Ener. 1 (2012) 401-412.

[26] K. Hashimoto, H. Irie, A. Fujishima, TiO_2 photocatalysis: a historical overview and future prospects, Jpn. J. Appl. Phys. 44 (2005) 8269-8285.

[27] N. Qin, Y. Liu, W. Wu, L. Shen, X. Chen, Z. Li, L. Wu, One-dimensional CdS/TiO_2 nanofiber composites as efficient visible-light-driven photocatalysts for selective organic transformation: synthesis, characterization, and performance, Langmuir 31 (2015) 1203-1209.

[28] X. Wang, Z. Li, J. Shi, Y. Yu, One-dimensional titanium dioxide nanomaterials: Nanowires, nanorods, and nanobelts, Chem. Rev. 114 (2014) 9346-9384.

[29] J.B. Priebe, M. Karnahl, H. Junge, M. Beller, D. Hollmann, A. Brückner, Water reduction with visible light: synergy between optical transitions and electron transfer in Au-TiO_2 catalysts visualized by in situ EPR spectroscopy, Angew. Chem. Int. Ed. 52 (2013) 11420-11424.

[30] G. Xie, K. Zhang, B. Guo, Q. Liu, L. Fang, J.R. Gong, Graphene-based materials for hydrogen generation from light-driven water splitting, Adv. Mater. 25 (2013) 3820-3839.

[31] V.M. Daskalaki, D.I. Kondarides, Efficient production of hydrogen by photo-induced reforming of glycerol at ambient conditions, Catal. Today 144 (2009) 75-80.

[32] N. Strataki, V. Bekiari, D.I. Kondarides, P. Lianos, Hydrogen production by photocatalytic alcohol reforming employing highly efficient nanocrystalline titania films, Appl. Catal., B Environ. 77 (2007) 184-189.

[33] S. McAllister, J.-Y. Chen, A.C. Fernandez-Pello, Fundamentals of Combustion Processes, Springer Science & Business Media, New York, NY, 2011.

[34] K. Zhang, Q. Liu, H. Wang, R. Zhang, C. Wu, J.R. Gong, TiO_2 single crystal with four-truncated-bipyramid morphology as an efficient photocatalyst for hydrogen production, Small 9 (2013) 2452-2459.

679 [35] S. Ray, J.A. Lalman, N. Biswas, Using the Box-Benkhen technique to statistically model
680 phenol photocatalytic degradation by titanium dioxide nanoparticles, Chem. Eng. J. 150 (2009)
681 15-24.
682 [36] J. Liu, Y. Liu, N. Liu, Y. Han, X. Zhang, H. Huang, Y. Lifshitz, S.T. Lee, J. Zhong, Z. Kang,
683 Metal-free efficient photocatalyst for stable visible water splitting via a two-electron pathway,
684 Science 347 (2015) 970-974.
685 [37] S.S. Veeravalli, S.R. Chaganti, J.A. Lalman, D.D. Heath, Optimizing hydrogen production
686 from a switchgrass steam exploded liquor using a mixed anaerobic culture in an upflow
687 anaerobic sludge blanket reactor, Int. J. Hydrogen Energ. 39 (2014) 3160-3175.
688 [38] S.R. Shanmugam, S.R. Chaganti, J.A. Lalman, D.D. Heath, Statistical optimization of
689 conditions for minimum H_2 consumption in mixed anaerobic cultures: effect on
690 homoacetogenesis and methanogenesis, Int. J. Hydrogen Energ. 39 (2014) 15433-15445.
691 [39] Y.-C. Pu, Y.-C. Chen, Y.-J. Hsu, Au-decorated $Na_xH_{2-x}Ti_3O_7$ nanobelts exhibiting
692 remarkable photocatalytic properties under visible-light illumination, Appl. Catal., B Environ. 97
693 (2010) 389-397.
694 [40] J. Zhang, Q. Xu, Z. Feng, M. Li, C. Li, Importance of the relationship between surface
695 phases and photocatalytic activity of TiO_2, Angew. Chem. Int. Ed. 47 (2008) 1766-1769.
696 [41] T. Kogure, T. Umezawa, Y. Kotani, A. Matsuda, M. Tatsumisago, T. Minami, Formation of
697 TiO_2(B) nanocrystallites in sol‐gel‐derived SiO_2‐TiO_2 film, J. Am. Ceram. Soc. 82 (1999)
698 3248-3250.
699 [42] Y.Q. Wang, G.Q. Hu, X.F. Duan, H.L. Sun, Q.K. Xue, Microstructure and formation
700 mechanism of titanium dioxide nanotubes, Chem. Phys. Lett. 365 (2002) 427-431.

701 [43] A. Chemseddine, T. Moritz, Nanostructuring titania: control over nanocrystal structure, size,
702 shape, and organization, Eur. J. Inorg. Chem. 1999 (1999) 235-245.
703 [44] G.L. Chiarello, E. Selli, L. Forni, Photocatalytic hydrogen production over flame spray
704 pyrolysis-synthesised TiO_2 and Au/TiO_2, Appl. Catal., B Environ. 84 (2008) 332-339.
705 [45] Z. Lai, M. Zhu, X. Yang, J. Wang, S. Li, Optimization of key factors affecting hydrogen
706 production from sugarcane bagasse by a thermophilic anaerobic pure culture, Biotechnol.
707 Biofuels 7 (2014) 131-111.
708 [46] A. Reungsang, S. Pattra, S. Sittijunda, Optimization of key factors affecting methane
709 production from acidic effluent coming from the sugarcane juice hydrogen fermentation process,
710 Energies 5 (2012) 4746-4757.
711 [47] M.A. Stephens, EDF statistics for goodness of fit and some comparisons, J. Am. Stat. Assoc.
712 69 (1974) 730.
713 [48] H. Cheng, J. Ma, Z. Zhao, L. Qi, Hydrothermal preparation of uniform nanosize rutile and
714 anatase particles, Chem. Mater. 7 (1995) 663-671.
715 [49] H. Zhang, J.F. Banfield, Understanding polymorphic phase transformation behavior during
716 growth of nanocrystalline aggregates: insights from TiO_2, J. Phys. Chem. B 104 (2000) 3481-
717 3487.
718 [50] M.C. Hidalgo, M. Maicu, J.A. Navío, G. Colón, Photocatalytic properties of surface
719 modified platinised TiO_2: effects of particle size and structural composition, Catal. Today 129
720 (2007) 43-49.
721 [51] G. Tian, H. Fu, L. Jing, B. Xin, K. Pan, Preparation and characterization of stable biphase
722 TiO_2 photocatalyst with high crystallinity, large surface area, and enhanced photoactivity, J. Phys.
723 Chem. C 112 (2008) 3083-3089.

[52] A. Monshi, M.R. Foroughi, M.R. Monshi, Modified Scherrer equation to estimate more accurately nano-crystallite size using XRD, World J. Nano Sci. Eng. 02 (2012) 154-160.

[53] H. Luo, C. Wang, Y. Yan, Synthesis of mesostructured titania with controlled crystalline framework, Chem. Mater. 15 (2003) 3841-3846.

[54] R. Lopez, R. Gomez, Band-gap energy estimation from diffuse reflectance measurements on sol–gel and commercial TiO_2: a comparative study, J. Sol-Gel Sci. Technol. 61 (2012) 1-7.

[55] J. Tao, T. Luttrell, M. Batzill, A two-dimensional phase of TiO_2 with a reduced bandgap, Nat. Chem. 3 (2011) 296-300.

[56] W. Fan, Q. Lai, Q. Zhang, Y. Wang, Nanocomposites of TiO_2 and reduced graphene oxide as efficient photocatalysts for hydrogen evolution, J. Phys. Chem. C 115 (2011) 10694-10701.

[57] I. Okura, M. Kaneko, Photocatalysis science and technology, Springer and Kodansha, Japan, 2002.

Optimizing one-dimensional TiO2 for photocatalytic hydrogen production from a water-ethanol mixture and other electron donors

Tao Peng, Jian Zhang, Srimanta Ray, Fatemeh Saadat Ghareh Bagh, Houssam Fakhouri, Farzaneh Arefi-Khonsari and Jerald A. Lalman